A EUROPEAN JOURNAL

CHEMPHYSCHEM

OF CHEMICAL PHYSICS AND PHYSICAL CHEMISTRY

Accepted Article

Title: Influence of orientational disorder on the optical absorption properties in hybrid metal-halide perovskite CH3NH3PbI3. A combined DFT/TD-DFT and experimental study.

Authors: Miłosz Adam Martynow, Damian Głowienka, Jędrzej Szmytkowski, Yulia Galagan, and Julien Guthmuller

To be cited as: *ChemPhysChem* 10.1002/cphc.201900824

Link to VoR: http://dx.doi.org/10.1002/cphc.201900824

A Journal of

ChemPubSoc Europe

WILEY-VCH

www.chemphyschem.org

Influence of orientational disorder on the optical absorption properties in hybrid metal-halide perovskite $CH_3NH_3PbI_3$. A combined DFT/TD-DFT and experimental study

Miłosz Martynow[1,*], Dr. Damian Głowienka[1], Dr. Jędrzej Szmytkowski[1], Dr. Yulia Galagan[2], Dr. Julien Guthmuller[1]

[1]*Faculty of Applied Physics and Mathematics, Gdańsk University of Technology, Narutowicza 11/12, 80-233 Gdańsk, Poland*

[2]*TNO – Solliance, High Tech Campus 21, Eindhoven 5656AE, The Netherlands*

Abstract

An experimental and theoretical investigation is reported to analyze the relation between the structural and absorption properties of $CH_3NH_3PbI_3$ in the tetragonal phase. More than 3000 geometry optimizations were performed in order to reveal the structural disorder and to identify structures with the lowest energies. The electronic structure calculations provide an averaged band gap of 1.674 eV, which is in excellent agreement with the experimental value of about 1.6 eV. The simulations of the absorption spectrum for three representative structures with lowest energy reproduced the absorption shoulders observed in the experimental spectra. These shoulders are assigned to excitations having similar orbital characters and involving transitions between hybridized 6s(Pb)/5p(I) orbitals and 6p(Pb) orbitals. The geometries of the three structures were analyzed and the effects of the inorganic frame and the $CH_3NH_3^+$ cations on the absorption properties were estimated. It was found that both changes in the inorganic frame and the $CH_3NH_3^+$ cations orientations impact the absorption spectra, by modifying the transitions energies and intensities. This highlights the

10.1002/cphc.201900824

role of $CH_3NH_3^+$ cation in influencing the absorption properties of $CH_3NH_3PbI_3$ and demonstrates that $CH_3NH_3^+$ cation is one of the key elements explaining the broad and nearly constant absorption spectrum in the visible range.

1. Introduction

Organic-inorganic hybrid perovskite materials have recently revolutionized the field of solar cell technology due to their high light-harvesting power conversion efficiency (PCE), excellent semiconductor properties of perovskite materials, simple manufacture and low cost of production (see *e.g.*[1]). A perovskite is a material with the chemical formula ABX_3 having the same type of crystal structure as calcium titanium oxide ($CaTiO_3$), in which A and B are two cations and X is an anion. The first perovskites containing organic molecules were synthesized in 1978 by Weber[2], which reported crystals of methylammonium lead halides ($CH_3NH_3PbX_3$ or $MAPbX_3$, where X is halide). The MA lead iodide ($MAPbI_3$), in particular, is probably the most important example of hybrid perovskite crystal. The first application of hybrid perovskites in a solar cell was reported in 2009 by Kojima *et al.*[3], which employed the perovskite compounds $MAPbI_3$ and $MAPbBr_3$ as photosensitizers, where a PCE of 3.8% was obtained for the $MAPbI_3$-based solar cell. Following this initial application, a lot of studies have been focused in the recent years on incorporating hybrid perovskite materials in solar cells due to their outstanding photovoltaic properties[4],[5],[6],[7],[8],[9],[10],[11],[12],[13],[14]. This has generated an exceptional increase in the solar cell efficiencies, which are currently exceeding 23%[15].

In parallel to the development of solar cells and to the increase of their efficiencies, a significant number of experimental and theoretical works have concentrated on understanding the fundamental properties of perovskite materials. In the case of $MAPbI_3$, these investigations have for example focused on the structural and electronic properties[16],[17],[18],[19],[20],[21] (band gap, band structure, dielectric constant, etc), the effects of the orientational disorder of the MA cations in the crystal structure[18],[22],[23],[24],[25],[26],[27],[28], the effects of temperature[29],[30],[31], the absorption spectrum[32],[33],[34],[35],[36], or the strong vibrational signal in IR and Raman spectra[37],[38]. $MAPbI_3$ is known to adopt three different

phases depending on the temperature[39],[40],[24], namely the orthorhombic phase is inherent below ~165 K, the tetragonal phase between ~165 K and ~327 K, and the cubic phase above ~327 K. In particular, the positional disorder of the MA cations increases with the temperature. Because the orientation of the MA cations is one of the most complex problems in the structural characterization of $MAPbI_3$, several theoretical studies have concentrated on the identification of the most stable structures, using static lattice calculations[17],[16],[32],[18],[41], as well as on the investigation of the dynamic structural distortions, using molecular dynamics (MD) simulations[22],[37],[26],[19],[42],[43],[44]. It has been established that the MA cations can freely rotate in the cubic phase, are partially hindered in the tetragonal phase (*e.g.* due to H-I hydrogen bonding) and can only liberate in the low temperature orthorhombic phase. Several preferred orientations of the MA cations were identified in the tetragonal phase[32],[18],[19],[44]. An additional essential characteristics of the $MAPbI_3$ is its excellent absorption properties characterized by a broad spectrum covering the whole visible region. It has been recognized that the orbital character of the valence band maximum is anti-bonding between I^- 5p and Pb^{2+} 6s orbitals, whereas the conduction band minimum has mostly non-bonding Pb^{2+} 6p orbital character slightly hybridized with I^- 5s orbitals[45],[32],[41]. However, there is little knowledge concerning the details of the allowed electronic transitions underlying the absorption spectrum and how these transitions are influenced by the changes in the inorganic crystal structure and by the orientational disorder of the MA cations.

This study has two objectives. Firstly, a systematic investigation of stable structures of $MAPbI_3$ in the tetragonal phase is performed using density functional theory (DFT) static lattice calculations. This is realized by optimizing more than 3000 $MAPbI_3$ structures in order to sample the orientational possibilities of the MA cations as well as the flexibility of the inorganic frame. Secondly, the absorption spectrum is measured experimentally for several film thicknesses and is simulated for different stable structures of $MAPbI_3$ using time

dependent DFT (TD-DFT) calculations in order to identify and assign the allowed electronic transitions. The paper is organized as follows: section 2 describes the experimental and theoretical methods. Section 3.1 presents the experimental characterization and optical properties of the $MAPbI_3$ films. Section 3.2 reports an investigation of the structural and electronic properties of the optimized crystal geometries. Section 3.3 provides the calculated absorption spectrum properties together with a comparison with the experimental results. Finally, section 4 presents the conclusion.

2. Methods

2.1 Experimental methods

Device preparation: The perovskite $CH_3NH_3PbI_3$ precursor was prepared using methylammonium iodide (MAI) powder (GreatCell Solar), lead iodide (PbI_2) powder (TCI) (99.99%), dimethylformamide (DMF) solvent (99.8%, Sigma-Aldrich) and 1-Methyl-2-pyrrolidinone (NMP) solvent (99.5%, ACROS Organics) without further purification. MAI and PbI_2 powders in equimolar ratio were dissolved in DMF:NMP (9:1 volume ratio) solvents mixture. The perovskite layer thickness variations were obtained with the use of 1 M, 1.2 M and 1.4 M molar concentrations in all experiments. All the solutions were stirred overnight at room temperature.

The patterned substrates with ITO have been cleaned in an ultrasonic bath, dried with N_2 gun and further treated with UV-Ozone (PR-100 UVIKON UV-Ozone) for 30 min. The following preparation of all solar cells was accomplished in glove-box with nitrogen environment where oxygen and moisture levels were kept at about 1 ppm. The spin-coating of the hole transporting layer (HTL) of poly(triaryl amine) (PTAA) (Sigma-Aldrich) dissolved in toluene with the concentration of 2 mg mL^{-1}. The PTAA solution was spin-coated at 5000 RPM for 35 s with the acceleration of 5000 RPM s^{-1} and further annealed at 100 ^oC. Subsequently, the perovskite 100 µL precursor was dynamically spin-coated at 2000 RPM for 10 s with 200 RPM s^{-1} acceleration and 5000 RPM for 30 s with 2000 RPM s^{-1}. After 15 s the N_2 gun was used for quenching of perovskite for 15 s and 6 bars pressure at 10 cm vertical distance from the substrate[46]. Afterwards, the perovskite samples were annealed on the hot-plate at 100 ^oC for 10 min. The electron transporting layers (ETLs) were prepared from fresh solution of [6,6]-Phenyl C61 butyric acid methyl ester (PCBM) (99%, Solenne) with 20 mg/mL concentration in chlorobenzene which was stirred overnight at 60^oC, and also bathocuproine (BCP) (99.99%, Sigma-Aldrich) dissolved in 0.5 mg mL^{-1} in ethanol. The spin-

coating of PCBM was done at 1500 RPM for 55 s with 3000 RPM s^{-1} acceleration and followed by spin-coating of BCP at 3000 RPM for 50 s with RPM s^{-1}. Subsequently, the ITO contacts were cleaned from all spin-coated layers with the use of DMF:chlorobenzene (1:6 volumetric ratio) solution. Finally, the 100 nm Au back contacts were deposited using vacuum (10^{-6} mbar) thermal evaporation method on the top of ETLs.

Characterization: The thickness of the films was measured using Bruker XT Dektak profiler. The structural characterization was investigated with X-ray diffractometer (XRD) (PanAlytical Empyrean). The atomic force microscope (AFM) (Park NX-10 tool) was used for studying morphology of the samples. UV-Vis absorption and PL emission measurements are used to investigate the optical properties of the sample. The UV-Vis spectrophotometer (Agilent Cary 5000) measured the transmittance (T) and the reflectance (R) using an integrating sphere to find the absorbance and absorption coefficient of the perovskite layer. The photoluminescence (PL) was measured (Horiba Labram Aramis system) with an excitation laser beam at 532 nm and Si detector. The J-V characteristics of the devices were measured in N_2 glove-box with simulated AM1.5 spectrum. The 100 mW cm^{-2} light intensity for the halogen lamp was calibrated using a Si reference cell. A stainless steel mask was used to define the active area (0.09 cm^2) of the samples. The J-V curves were measured in forward and reverse bias with Keithley 2400 with a scanning rate of 165 mV ms^{-1} with 20 mV step. The Rera Solutions setup was used to measure the external quantum efficiency (EQE).

2.2 Theoretical and computational methods

All the calculations have been realized using version 6.1 of the Quantum Espresso package[47]. Structural optimizations were performed at the DFT level of theory using the PBE exchange-correlation functional[48] and the Broyden-Fletcher-Goldfarb-Shanno algorithm as implemented in the PWscf code. Ultrasoft scalar relativistic pseudopotentials were employed,

that is, the electrons from the Pb 5d, 6s, 6p; I 5s, 5p; C and N 2s, 2p; and H 1s, shells are treated explicitly. The optimizations are performed on a tetragonal unit cell containing in total 48 atoms with 4 MA cations and using cell parameters fixed to the experimental values[49] at 293 K, namely a = b = 8.849 Å and c = 12.642 Å (Figure 1). Thresholds of 10^{-4} Ry and 10^{-3} a.u. were applied for the total energy and the forces, respectively. Additionally, the kinetic energy cutoffs for the wavefunction (E_Ψ) and the charge density (E_ρ) were set to E_Ψ = 36 Ry and $E_\rho = 14 \times E_\Psi$ = 504 Ry, respectively. These values are based on self-consistent field calculations (SCF) realized on a test structure and provide a reasonable computational time as well as an accuracy of about 10^{-2} eV on the total energy (see Figures S1 and S2). Moreover, due to the lack of symmetry in the analyzed $MAPbI_3$, a regular Monkhorst and Pack (MP) k-point mesh was set for the Brillouin zone integration[50]. Its effects on the total energy, on the band gap, on the geometry and on the computational time were estimated by test calculations performed with an increasing number of k-points, namely ranging from Γ point (k = 1) calculation, which was named for clarity Low Resolution (LR) calculations, up to resolution with a 7 × 7 × 7 grid (k = 172) (see Figures S3 and S4). Based on these tests, the most stable structures of $MAPbI_3$ were determined with geometry optimizations realized in three steps, which provide a reasonable compromise between accuracy and computational cost. Firstly, more than 3000 initial structures were generated by rotating the MA cations along their C-N axis with a step size of 15° and by orienting the C-N bond either in the positive or negative direction of the z crystal axis. All these structures were optimized with Γ point calculations. Secondly, the 100 initial structures, which gives lowest total energies in the first step were re-optimized with Medium Resolution (MR) calculations using a 3 × 3 × 3 MP mesh (k = 13). These calculations allow the identification of an ensemble of structures having relative total energies of the order of the thermal energy at room temperature (kT = 26 meV at T = 300 K). Finally, High Resolution (HR) geometry optimizations were performed using a 6 × 6 × 6 MP

k-point mesh (k = 112) for the six most stable structures obtained in the second step. The 6 × 6 × 6 grid provides a better convergence of the band gap value (see Figure S3) and is employed to estimate the numerical errors on the geometries and the total relative energies.

The absorption spectrum of $MAPbI_3$ was predicted using Γ point TD-DFT calculations as implemented in the turboTDDFT code[51],[52] with the Turbo Davidson algorithm. These calculations were performed on three structures optimized with the 6 × 6 × 6 grid, illustrating the different orientations that the MA cations can adopt. The properties of 150 excited states were calculated, which provided a simulation of the absorption spectrum in the entire visible region.

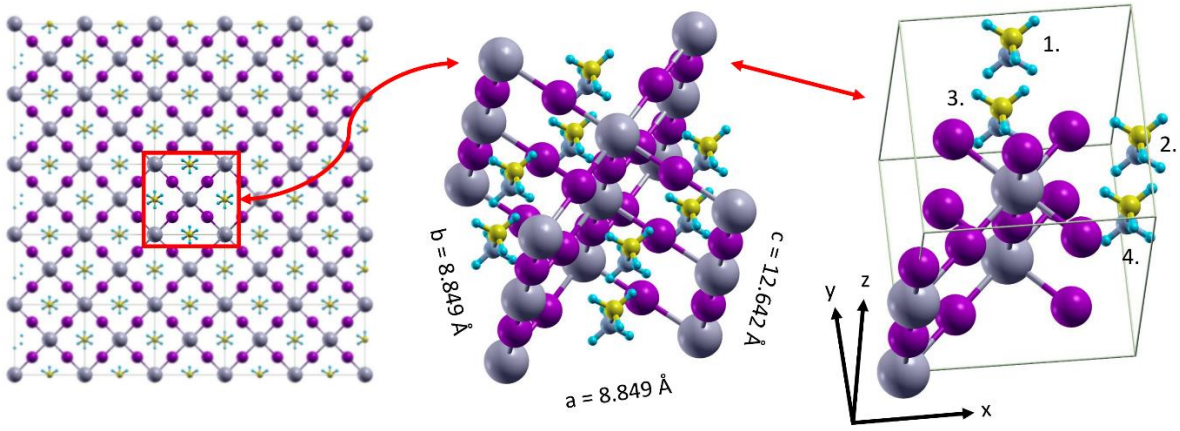

Figure 1. Tetragonal unit cell used to generate the initial structures of $MAPbI_3$ by rotation of the four MA cations. I, Pb, N, C and H atoms are indicated in magenta, dark-gray, light-gray, yellow and blue colors, respectively.

3. Results

3.1 Experimental results

The thickness of each $MAPbI_3$ layer was measured with a profilometer giving 375±5 nm, 470±2 nm and 575±4 nm for molar concentrations of 1 M, 1.2 M and 1.4 M, respectively. In the following studies, the three layers are referred with respect to their thickness (375 nm, 470 nm and 575 nm) instead of their molar concentration. The crystal structure and phase has been characterized with the XRD measurements. Figure 2(a) shows the XRD results of $MAPbI_3$ for three thicknesses with negligible differences in respect to three measured samples. The structures show tetragonal phase with the *I4cm* symmetry and the highest intensity for the (110) diffraction peak[53]. A very low amount of secondary PbI_2 phase is also observed, which is related to negligible diffraction peak at 13^o. The morphology of $MAPbI_3$ on the glass is analyzed with AFM measurements (see Figure S5). The perovskite layers have large grains size equal to approximately 213 nm (analysis performed on about 100 grains) for all samples with a very good coverage. The RMS roughness of the samples is equal to 7.8 nm, 11.3 nm and 11.51 nm for 375 nm, 470 nm and 575 nm thicknesses, respectively.

The optical analysis has been performed with UV-Vis and PL measurements, as shown in Figure 2. The UV-Vis results have been obtained by measurements of the transmission (T) and reflectance (R) of the perovskite layers in order to calculate absorbance (100%=A+T+R), see Figure 2(b). The experimental spectra show maximum absorbance peaks at about 440 nm, 550 nm, 660 nm and 740 nm, which are especially visible for the lowest thickness of the film. Figure 2(c) shows the absorption coefficient also calculated using the transmission and reflectance results. The data from the Tauc plot is used to calculate the optical band gap, see Figure 2 (c-inset). E_g is equal to 1.614 eV, 1.606 eV and 1.600 eV for the 375 nm, 470 nm and 575 nm thicknesses, respectively. The same shift of a band gap in a function of the film thickness is also observed for a maximum of PL intensity measurements. This is explained

with the theory of in–plane tensile strain which are perpendicular to the perovskite layer and increases with the thickness which lead to the change of the band–gap[54].

The perovskite solar cells (PSCs) have been prepared with the same perovskite layer thickness as discussed earlier. The devices were prepared in ITO/PTAA/perovskite/PCBM/BCP/Au inversed p-i-n structure. The PSCs have been measured under AM1.5 light intensity, see Figure 3(a). The hero cells show efficiency equal to 15.67%, 15.14% and 14.49% for thicknesses of 375 nm, 470 nm, and 575 nm, respectively. The final efficiency decreases with the observed lowering of fill-factor (FF), open-circuit voltage (V_{oc}) and short-circuit photocurrent (J_{sc}) for each film thickness. As shown in Figure S6, the hysteresis of PSC is very small for each device, however, it slightly increases with film thickness. The low hysteresis level in PSCs indicates a good quality of layer, which is crucial for further simulation analysis. In Figure 3(b), the EQE results for the same PSCs follow absorbance spectrum from UV-Vis results with the approximately same absorption peaks. The small differences could result in optical reflection effects. The photocurrent curve is calculated by integration over wavelength and it shows total current close to J_{sc} obtained in J-V curves.

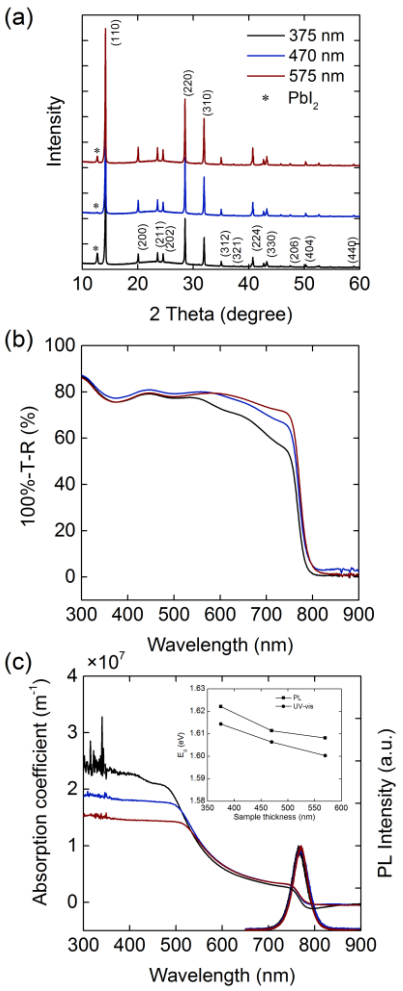

Figure 2. $MAPbI_3$ characterization on glass with: a) X-ray diffraction (XRD), b) UV-Vis measurements, and c) absorption coefficient with PL measurements. The inset of part (c) includes the band gap relation to thickness of perovskite film based on UV-Vis and PL measurements. Black, blue and red colors represent 375 nm, 470 nm and 575 nm thicknesses of perovskite, respectively.

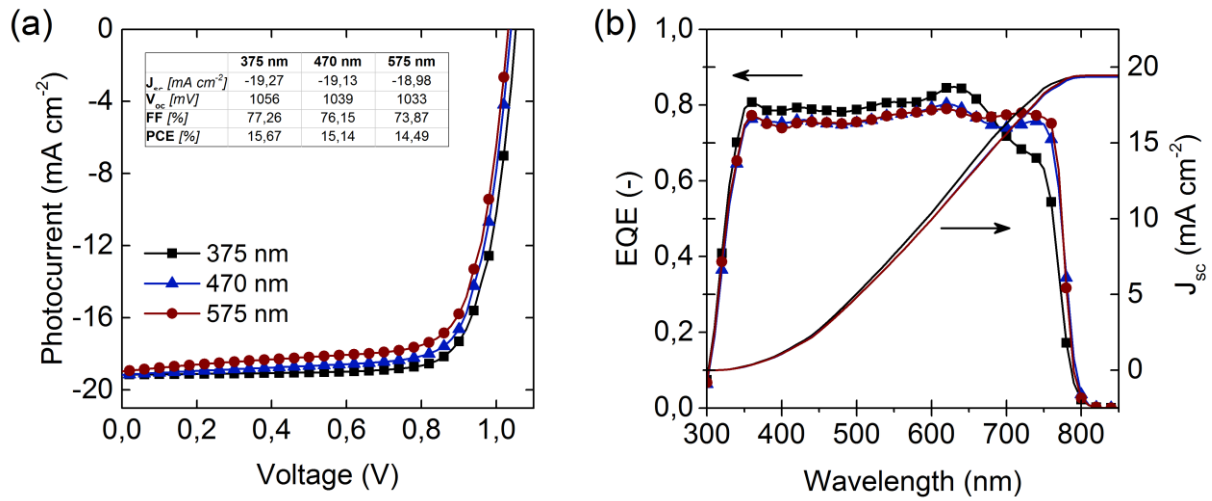

	375 nm	470 nm	575 nm
J_{sc} [mA cm^{-2}]	-19,27	-19,13	-18,98
V_{oc} [mV]	1056	1039	1033
FF [%]	77,26	76,15	73,87
PCE [%]	15,67	15,14	14,49

Figure 3. Experimental results of perovskite solar cells. a) J-V characteristics, and b) EQE measurements. Black (square), blue (upper triangle) and red (circle) colors represent 375 nm, 470 nm and 575 nm thicknesses of perovskite layer, respectively.

3.2 Structural and electronic properties

To provide a sampling of the possible MA orientations, 3162 initial geometries of $MAPbI_3$ were generated by rotating the four MA cations within the inorganic framework displayed in Figure 1. Then, these structures were optimized without constraints by LR (i.e. Γ point) calculations. This generates a distribution of stationary geometries having different orientations of the MA cations and including the relaxation effects on the inorganic frame. These structural differences impact the electronic properties of $MAPbI_3$. In particular, the relation between the total energy of the geometries and the band gap is presented in Figure 4. The optimized structures display a broad distribution of total energies having differences larger than 0.1 Ry (i.e., 1.36 eV). Moreover, several geometries with nearly identical total energies show very different band gap values. The distribution of structures with respect to the band gap can be approximated by a bell-shaped curve with a mean value at 2.383 eV and a standard deviation (σ) of 0.119 eV (Table 1). The calculated band gap is significantly overestimated in comparison to the experimental value of about 1.6 eV (see section 3.1). This disagreement can be ascribed to the use of LR calculations, whereas MR and HR calculations provide band gap values lower in energy by about 0.7 eV (see Figure S3). Similarly, MR or HR calculations are required to reach convergence for the total energy, which is decreased by more than 0.1 Ry going from LR to MR calculations. In the next step, the 100 lowest energy geometries were re-optimized with MR calculations (Figure 5). At the LR level of theory, these structures cover an energy range of almost 0.03 Ry (i.e., 0.408 eV), which is significantly larger than the thermal energy at room temperature (kT = 0.026 eV). Therefore, it can be assumed that these 100 structures contain a realistic ensemble of stationary geometries accessible at 300K in the tetragonal phase of $MAPbI_3$. However, it cannot be excluded that some low-energy structures might be missing due to two reasons (i) the limits in

the sampling (e.g. finite rotation steps) of the MA cations orientation used in the generation of the initial geometries and (ii) the fact that higher energy geometries in the LR calculation might relax at lower energies in the MR calculations. The calculated mean value of the band gap for the MR geometries is 1.563 eV, whereas it is increased to 1.674 eV when assuming a Boltzmann distribution at 300 K. This difference originates from the fact that the lowest energy structures have larger band gap values than higher energy structures (Figure 5). The calculated band gap values are in excellent agreement with the experimental value (i.e., 1.6 eV). Nevertheless, although non-relativistic DFT calculations were shown to be accurate for the structural properties[20], it was also previously recognized[34] that the agreement for the band gap is the result of a cancellation of errors occurring from the neglect of spin-orbit couplings (decreasing the band gap) and from the missing correlation effects in the DFT approximation (increasing the band gap). Additionally, Figure 5 shows that the six lowest geometries are comprised in an energy range of about 0.003 Ry (i.e., 0.041 eV) corresponding to about 1.5 kT (i.e., 0.039 eV) at room temperature, whereas the other structures are found with energies of more than 0.008 Ry (i.e., 0.11 eV) above the global minimum. These six geometries were re-optimized using HR calculations in order to check the convergence of the results. Thus, going from MR to HR calculations has the effect of lowering their mean total energy by about 0.001 Ry and of decreasing their mean band gap value by 0.01 eV (Table 1). This shows that the results are nearly converged and that larger k-point mesh are not necessary.

Table 1. Mean values (μ) and standard deviations (σ) of the total energy and band gap calculated for various numbers of structures and different resolutions.

Resolution	Number of structures	Total energy (Ry)		Band gap (eV)	
		μ	σ	μ	σ
LR	3162	-1452.264893	0.019074	2.383	0.119
	100	-1452.296966	0.005463	2.441	0.101
	6	-1452.297770	0.004579	2.396	0.061
MR	100	-1452.385690	0.015634	1.563	0.172
	6	-1452.400683	0.001070	1.668	0.050
HR	6	-1452.401554	0.000900	1.658	0.043

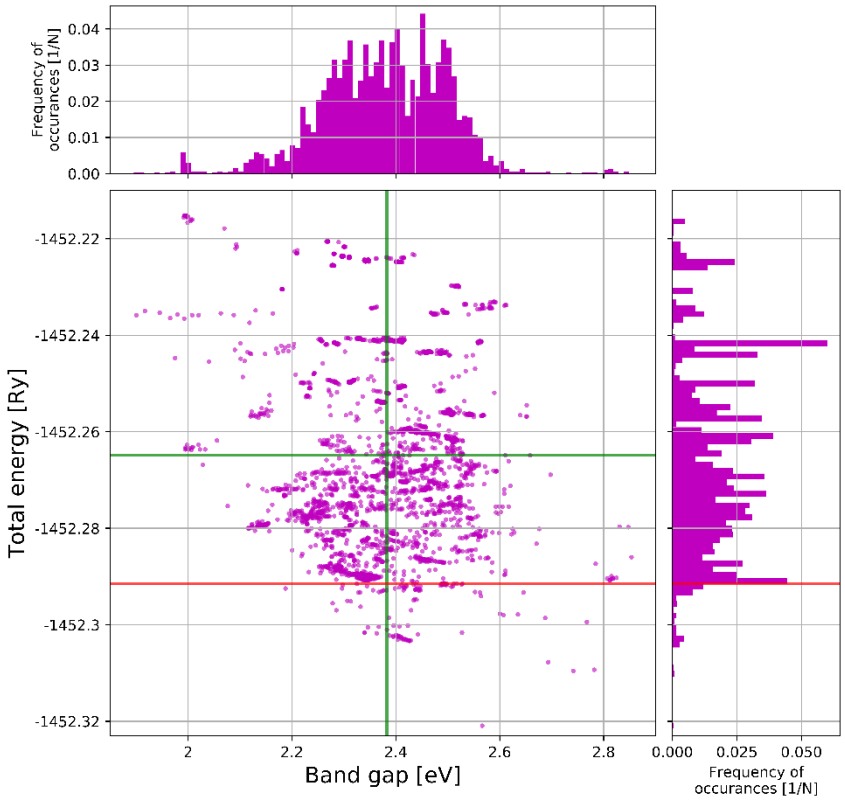

Figure 4. Relation between the total energy and the band gap for the 3162 LR optimized geometries. The vertical and horizontal green lines indicate the mean values of the band gap and total energy, respectively. The red line indicates the threshold employed for the selection of the 100 structures optimized with MR. Bin widths of 0.01 eV and 0.0012 Ry were employed for the band gap and total energy histograms, respectively.

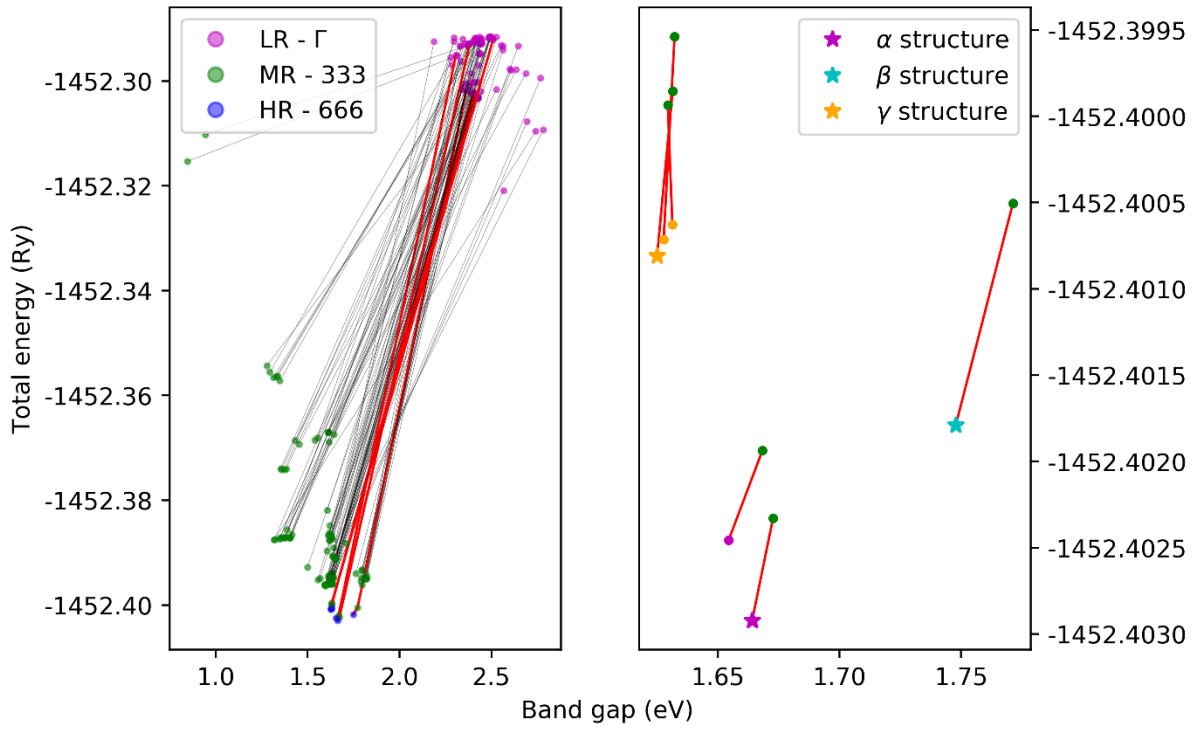

Figure 5. (left) Connections (black lines) between the 100 lowest structures calculated at LR (magenta circles) and at MR (green circles). The 6 geometries optimized at HR are indicated by blue circles and

their connections to MR and LR structures are given by red lines. (right) Focus on the 6 lowest geometries, the three structures (α, β and γ) investigated for absorption are indicated by stars.

The analysis of the six lowest energy structures reveals that the two lowest structures have comparable orientations of the MA cations (e.g., differences of less than 5° for the orientational angles, see Table S1) and comparable inorganic frame geometries. Similarly, the three higher energy structures have comparable geometries, which can be associated with their close energies and band gaps (Figure 5). Therefore, only three structures named α, β and γ (Figures 5 and 6) are considered in the following to assess the impact of geometrical modifications on the optical properties. Figure 6 presents a comparison of the α, β and γ geometries. It is seen that the tilting of the PbI_6 octahedrons are nearly similar for the three structures in the YZ plane, whereas differences in the inorganic frame geometries are observed in the XY and XZ planes. In particular, the α and γ inorganic structures are closer to one another with the comparable rotation of the octahedrons along the Z axis (see XY plane) and almost no tilting of the octahedrons in the XZ plane. This differs from the β structure, in which the octahedrons have almost no rotation along the Z axis and are tilted in the XZ plane. The differences in the inorganic frame are quantified by the four dihedral angles D_1, D_2, D_3 and D_4 (Figure 7 and Table 2). The D_1 and D_3 angles describe rotations of the octahedrons along the Z crystal axis, while D_2 and D_4 describe rotations related to the tilting of the octahedrons. The dihedral angles of the α and γ structures differ by at most 3°, whereas the D_1/D_3 and D_2/D_4 angles of the β structure are about 6 to 10° smaller and 10 to 13° larger than for the other two structures, respectively (Table 2). Hence, the α and γ structures have more rotated octahedrons along the Z axis than the β structure, and the β structure has larger tilting of the octahedrons than α and γ structures. Then, the orientations of the four MA cations were characterized by the projection on the crystal axes of a unit vector oriented along with the C-N bond (Table 2). A similar approach was employed in a previous molecular dynamics

study[44]. It is seen that both α and γ structures have two MA cations (although not the same) oriented along the X axis ($|P_X| > 0.95$) and two MA cations having components in the three axis directions with a principal projection along the Z axis ($|P_Z| = 0.72\text{-}0.77$). The four MA cations of the β structure have components in the three axis directions with a dominant projection along the Z axis ($|P_Z| = 0.83\text{-}0.90$). This shows that the β structure differs from the α and γ structures both in the inorganic frame and in the orientations of the MA cations.

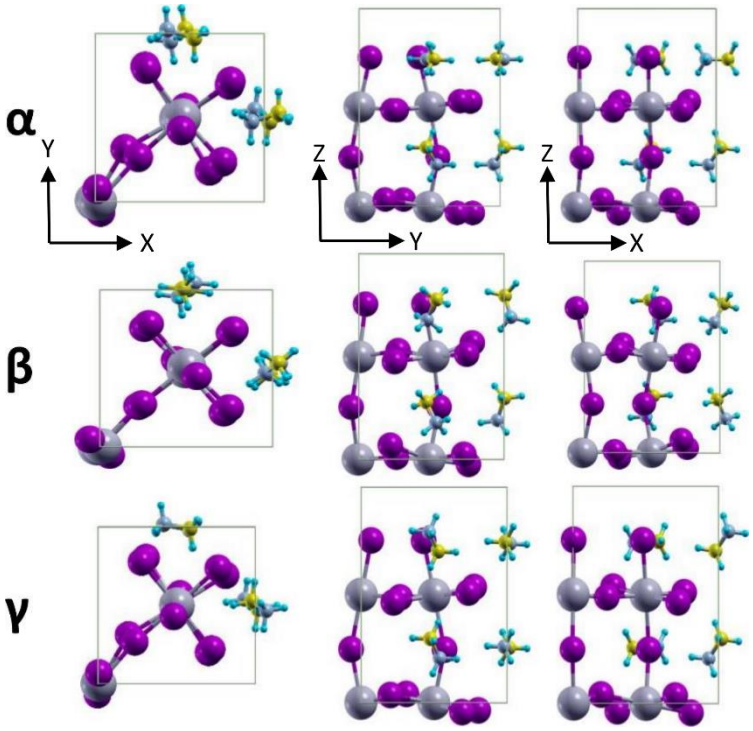

Figure 6. Views of the α, β and γ structures along the XY (left), YZ (middle) and XZ (right) crystal planes.

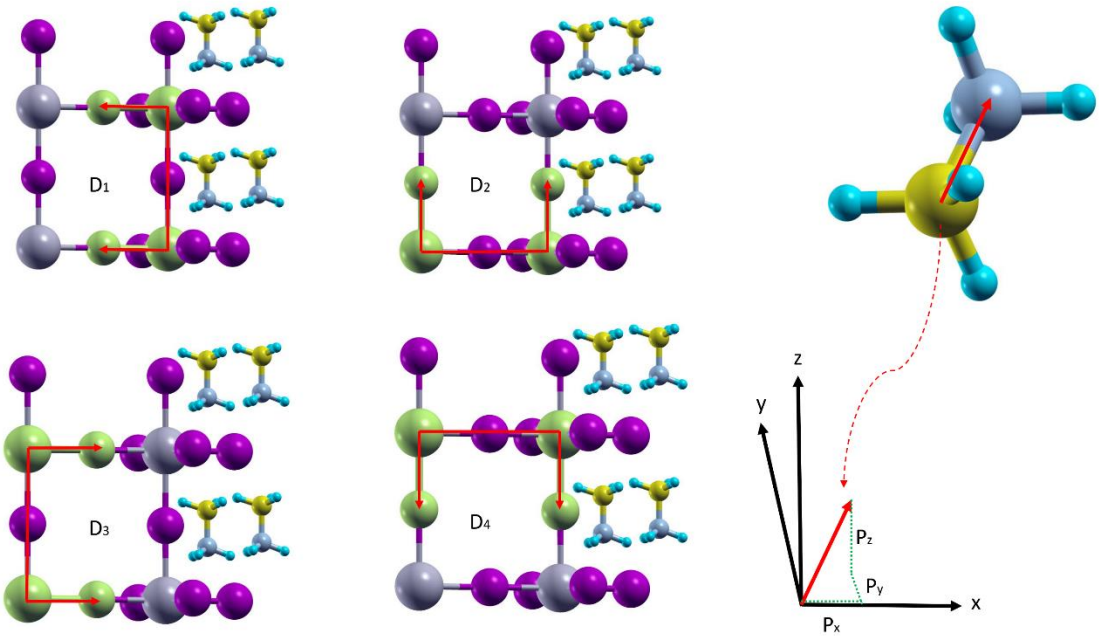

Figure 7. Definition of the four considered dihedral angles D_1, D_2, D_3 and D_4 describing the inorganic frame as well as the three projections P_X, P_Y, and P_Z describing the MA cations orientations.

Table 2. Dihedral angles (D_i) and projections (P_I) of the α, β and γ structures.

Parameter	Structure		
	α	β	γ
	Inorganic frame dihedral angle (°)		
D_1	12.7	3.5	9.6
D_2	14.6	26.6	12.9
D_3	11.6	1.5	9.6
D_4	12.9	23.1	13.4
	Molecule 1 projection		
P_X	-0.95	-0.39	-0.98
P_Y	-0.31	-0.23	0.18
P_Z	-0.03	-0.89	-0.06
	Molecule 2 projection		
P_X	-0.95	-0.41	0.53
P_Y	0.31	0.38	-0.37
P_Z	0.00	0.83	0.76
	Molecule 3 projection		
P_X	-0.53	0.33	-0.98
P_Y	-0.44	-0.28	-0.20
P_Z	-0.72	0.90	-0.04
	Molecule 4 projection		
P_X	-0.51	-0.36	-0.51
P_Y	0.42	-0.40	0.38
P_Z	-0.75	0.84	-0.77

3.3 Optical properties

The experimental UV-Vis absorption spectra of the $MAPbI_3$ samples (Figure 2) present the typical sharp increase of absorbance close to 775 nm (~1.6 eV), which leads to an absorbance of about 70-80% in the 775-300 nm region. However, the measured UV-Vis spectra also display variations in the absorbance with shoulders at about 740, 660, 550 and 440 nm (see section 3.1). Therefore, TD-DFT calculations of the absorption spectra were performed for the α, β and γ structures (Figure 8) in order to decipher the origin of the experimental absorption features. These calculations were performed at the Γ point by employing the HR optimized structures. The use of Γ point calculations can be justified by electronic band structure calculations realized with a 10 k-point grid along each high symmetry lines (see Figure S7). Similarly to previous reports[55],[56] our results show that for the three α, β and γ structures the lowest energy gap (i.e., the difference between the conduction and valence bands) always occurs at the Γ point, whereas other high symmetry

points present larger energy differences. This indicates that the lowest electronic transitions present in the absorption spectrum should predominantly occur at the Γ point.

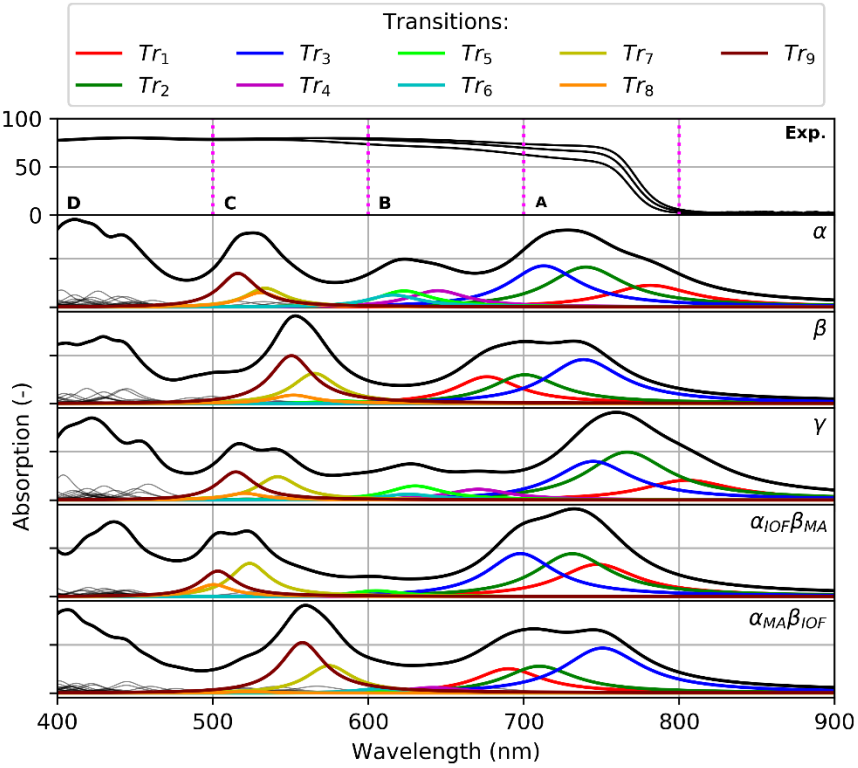

Figure 8. Absorption spectra of $MAPbI_3$. Experimental spectra for a thickness of 375 nm and calculated spectra for the α, β, γ, $\alpha_{IOF}\beta_{MA}$ and $\alpha_{MA}\beta_{IOF}$ structures. A, B, C and D indicate the four considered spectral regions. The transitions are broadened with a Lorentzian function of full width at half maximum of 0.005 Ry, the nine main transitions are indicated in colors.

To facilitate the interpretation of the absorption spectrum, it is divided into four wavelength regions, namely A=700-800 nm, B=600-700 nm, C=500-600 nm and D=400-500 nm (Figure 8). The spectral region A of the α and γ structures is dominated by three transitions (referred as Tr_1, Tr_2 and Tr_3) forming a first absorption band. Tr_1, Tr_2 and Tr_3 involve transitions from the highest occupied orbital $O_0[p_{//}(I)s(Pb)]$ to the unoccupied orbitals $O_1[p_Z(Pb)]$ (i.e., lowest unoccupied orbital), $O_2[p_Y(Pb)]$ and $O_3[p_X(Pb)]$, respectively (Figure 9 and Table 3). The O_0 orbital character is anti-bonding between the Pb 6s orbital and the I 5p orbitals oriented parallel to the Pb-I bonds, whereas the O_1, O_2 and O_3 orbitals characters correspond mainly to Pb 6p orbitals (Figure 9). The energetic order of the three transitions is identical in both α and γ structures, while the transitions are slightly red-shifted for γ and a

change of relative intensities is obtained for the Tr_2 and Tr_3 transitions (Figure 8). The β structure presents the same three transitions at lower energies. However, their energetic order and positions are significantly different than for the α and γ structures. In particular, the Tr_1 transition is the lowest in the α (at 781 nm) and γ (at 805 nm) structures, whereas it is blue-shifted to the B spectral region for the β structure (at 676 nm), in which it becomes the third transition. This difference is associated with a modification of the orbital energetic order, namely the $O_1[p_Z(Pb)]$ orbital is the lowest unoccupied orbital in the α and γ structures, whereas the orbital energetic order is $O_3[p_X(Pb)]$, $O_2[p_Y(Pb)]$ and $O_1[p_Z(Pb)]$ for the β structure. These results are in general agreement with the differences of geometries described in section 3.2, i.e., the α and γ structures share comparable geometrical and absorption features, whereas the β structure presents a different absorption spectrum due to a noticeable different geometry. Additional TD-DFT calculations were performed for the two structures $\alpha_{IOF}\beta_{MA}$ and $\alpha_{MA}\beta_{IOF}$ (Figure 8) in order to identify if the changes in absorption properties between the α and β structures originate from the inorganic frame (IOF) or from the orientation of the MA cations. $\alpha_{IOF}\beta_{MA}$ corresponds to a structure having the same IOF as the α structure and the same MA cations orientations as the β structure, while $\alpha_{MA}\beta_{IOF}$ has the IOF of β and the MA cations orientations of α. It is seen from Figure 8 and Table 3 that the Tr_1, Tr_2 and Tr_3 transitions properties of the $\alpha_{IOF}\beta_{MA}$ and $\alpha_{MA}\beta_{IOF}$ structures are very close to the properties of the α and β structures, respectively. This demonstrates that the spectral changes between the α and β structures mainly originate from the modifications of the IOF and that the MA cations orientations have only a minor effect on the absorption properties in this region. In particular, the larger tilting of the octahedrons in the β structure in comparison to the α structure (see section 3.2) is expected to affect the overlap between the s(Pb), p(I) and p(Pb) orbitals and consequently to modify their stability as well as the energies of the transitions in which these orbitals are involved.

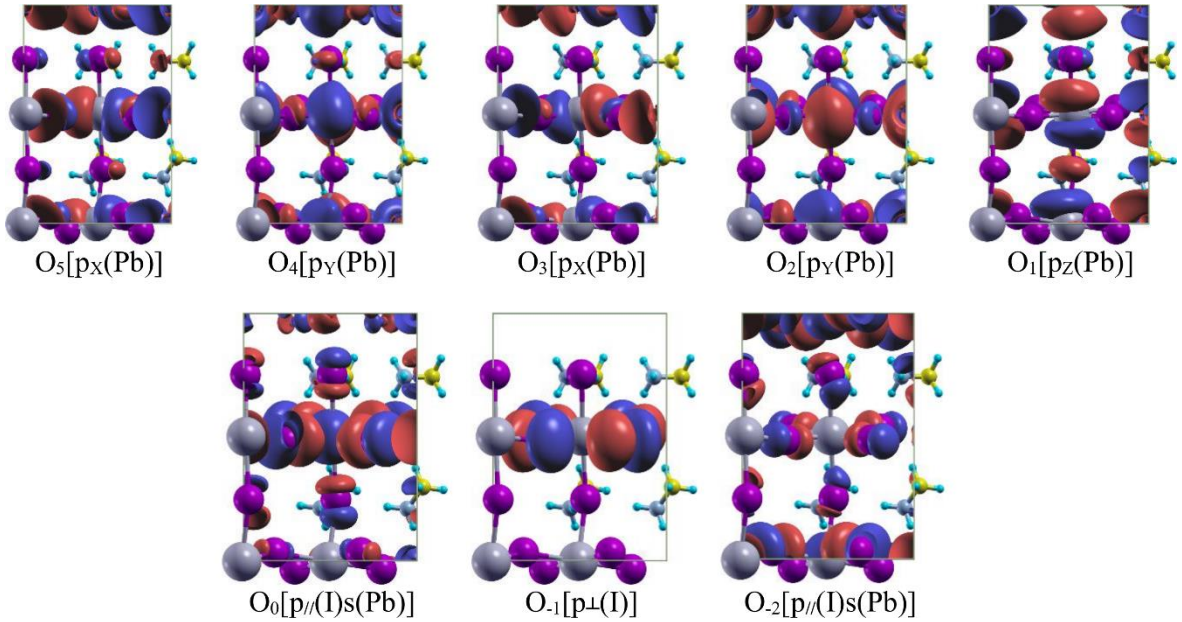

Figure 9 Main orbitals involved in the absorption properties. Numbers from -2 to 0 and from 1 to 5 indicate the occupied and unoccupied orbitals, respectively. The orbitals are represented for the α structure in the XZ plane.

The spectral region B displays less intense transitions than region A. Similarly to the observations made for region A, the α and γ structures have comparable spectral feature in region B, i.e., forming an absorption band obtained from the overlap of mainly three transitions (Tr_4, Tr_5 and Tr_6), whereas the β structure has very small intensities in this spectral region (with the exception of Tr_1). This second band in the simulated absorption spectra of the α and γ structures can be assigned to the experimental shoulder at 660 nm. Tr_4, Tr_5 and Tr_6 involve transitions between the occupied $O_{-2}[p_{//}(I)s(Pb)]$ and $O_0[p_{//}(I)s(Pb)]$ orbitals and the unoccupied $O_1[p_Z(Pb)]$, $O_4[p_Y(Pb)]$ and $O_5[p_X(Pb)]$ orbitals (Figure 9 and Table 3). The orbitals O_{-2}, O_4 and O_5 mostly differ from the orbitals O_0, O_2 and O_3 by a different phase sign of the p(I) or p(Pb) orbitals. Therefore, Tr_4, Tr_5 and Tr_6 describe transitions with similar orbital characters as the three transitions present in the region A (Tr_1, Tr_2 and Tr_3). The investigation of the $\alpha_{IOF}\beta_{MA}$ system shows that the intensities of all three transitions are significantly decreased respectively to the α structure (Figure 8 and Table 3). This change is consequently attributed to the modification of MA cations orientations (β_{MA} decrease the

intensities in this case). However, for the $\alpha_{MA}\beta_{IOF}$ structure, the Tr_4 and Tr_6 intensities are increased and the Tr_5 intensity is slightly decreased when comparing to the β structure. This illustrates again the effect the MA cations orientations have on the absorption intensities (α_{MA} mainly increases the intensities in this case). Therefore, it appears that in the spectral region B both the modification of the IOF and of the MA cations orientations impact equivalently the absorption properties. The relatively larger effect of the MA cations in the region B in comparison to the region A is probably due to the stronger intensities in the region A, which are consequently relatively less affected by the interaction with the MA cations. It is also possible that the higher lying orbitals O_4 and O_5, involved in Tr_4 and Tr_5, are more sensitive to the interaction with the MA cations.

The spectral region C displays an absorption band formed mainly by the three transitions Tr_7, Tr_8 and Tr_9 (Figure 8 and Table 3). This band is present in the three structures α, β and γ and can be assigned to the experimental shoulder at 550 nm. The following observations can be made, (i) the β structure band is red-shifted in comparison to the α and γ structures bands, (ii) the orbital characters of the transitions are similar to the orbital characters obtained in the regions A and B (with some exception for Tr_8 in the β and $\alpha_{IOF}\beta_{MA}$ structures, see Table 3 and Figure S8), and (iii) the results for $\alpha_{IOF}\beta_{MA}$ structure show that MA cations orientations have an impact on the relative intensities of the Tr_8 and Tr_9 intensities, whereas the absorption band for $\alpha_{MA}\beta_{IOF}$ structure is very similar to the β structure indicating a stronger effect of the IOF when going from the α to the β structure. The spectral region D shows an additional band for all considered structures and can be assigned to the experimental shoulder at 440 nm. This band is formed by a complicated overlap of several transitions and is consequently not analyzed in details.

Table 3. Excitation wavelengths (λ), absorption strengths (χ), electronic transitions and weights (%) of the main singlet transitions of the α, β, λ, $\alpha_{IOF}\beta_{MA}$ and $\alpha_{MA}\beta_{IOF}$ structures.

Transition	Structure	Transition [a]	Weight (%)	λ (nm)	χ
Tr_1	α	$O_0[p_{//}(I)s(Pb)] \rightarrow O_1[p_Z(Pb)]$	≈100	781.4	4.406
	β		≈100	676.3	5.557
	γ		≈100	804.9	4.725
	$\alpha_{IOF}\beta_{MA}$		≈100	747.4	6.566
	$\alpha_{MA}\beta_{IOF}$		≈100	690.1	4.962
Tr_2	α	$O_0[p_{//}(I)s(Pb)] \rightarrow O_2[p_Y(Pb)]$	≈100	739.9	7.675
	β		≈100	700.7	6.178
	γ		≈100	766.5	10.904
	$\alpha_{IOF}\beta_{MA}$		≈100	731.2	8.553
	$\alpha_{MA}\beta_{IOF}$		≈100	710.0	5.645
Tr_3	α	$O_0[p_{//}(I)s(Pb)] \rightarrow O_3[p_X(Pb)]$	≈100	712.8	7.614
	β		≈100	738.4	9.948
	γ		≈100	744.6	8.536
	$\alpha_{IOF}\beta_{MA}$		≈100	697.8	8.186
	$\alpha_{MA}\beta_{IOF}$		≈100	750.6	9.989
Tr_4	α	$O_0[p_{//}(I)s(Pb)] \rightarrow O_4[p_Y(Pb)]$	98	644.6	2.746
	β		63	633.5	0.001
	γ		99	670.7	2.143
	$\alpha_{IOF}\beta_{MA}$		97	632.1	0.278
	$\alpha_{MA}\beta_{IOF}$	$O_{-2}[p_{//}(I)s(Pb)] \rightarrow O_2[p_Y(Pb)]$	79	641.8	1.045
Tr_5	α	$O_{-2}[p_{//}(I)s(Pb)] \rightarrow O_1[p_Z(Pb)]$	82	622.9	2.614
	β		97	582.3	0.488
	γ		82	630.1	2.640
	$\alpha_{IOF}\beta_{MA}$		78	599.4	0.958
	$\alpha_{MA}\beta_{IOF}$		93	605.0	0.229
Tr_6	α	$O_0[p_{//}(I)s(Pb)] \rightarrow O_5[p_X(Pb)]$	47	615.8	1.930
	β		97	608.7	0.033
	γ		84	625.7	1.092
	$\alpha_{IOF}\beta_{MA}$		77	523.7	0.246
	$\alpha_{MA}\beta_{IOF}$		96	608.4	0.784
Tr_7	α	$O_{-2}[p_{//}(I)s(Pb)] \rightarrow O_4[p_Y(Pb)]$	61	533.6	2.610
	β		91	565.3	5.222
	γ		75	541.6	3.755
	$\alpha_{IOF}\beta_{MA}$		81	523.7	4.736
	$\alpha_{MA}\beta_{IOF}$		95	574.8	4.665
Tr_8	α	$O_{-1}[p_{\perp}(I)] \rightarrow O_5[p_X(Pb)]$	80	530.8	1.991
	β	$O_{-3}[p_{\perp}(I)] \rightarrow O_3[p_X(Pb)]$	91	551.9	1.430
	γ		93	520.2	1.046
	$\alpha_{IOF}\beta_{MA}$	$O_{-1}[p_{\perp}(I)] \rightarrow O_4[p_Y(Pb)]$	81	500.6	1.632
	$\alpha_{MA}\beta_{IOF}$		65	523.8	0.215
Tr_9	α	$O_{-2}[p_{//}(I)s(Pb)] \rightarrow O_5[p_X(Pb)]$	92	516.1	4.516
	β		92	550.5	8.072
	γ		98	514.8	4.300
	$\alpha_{IOF}\beta_{MA}$		89	503.2	3.493
	$\alpha_{MA}\beta_{IOF}$		97	557.6	8.340

[a] If not indicated otherwise, the main transition is similar to the α structure.

4. Conclusions

An experimental and theoretical investigation of the structural and absorption properties of $MAPbI_3$ has been conducted. More than 3000 geometries were optimized with LR calculations in order to sample the MA cations orientation and the IOF structure. MR optimizations provided an ensemble of stationary geometries accessible at 300K in the tetragonal phase of $MAPbI_3$. Assuming a Boltzmann distribution, the band gap is calculated at 1.674 eV, which is in excellent agreement with the experimental value of about 1.6 eV. Additionally, the calculated standard deviations of about 0.1-0.2 eV provide an estimate of the band gap sensitivity to the changes in geometry. Then, three structures of lower energy (α, β and γ) were considered to assess the effects of geometrical modifications on the electronic and absorption properties. First, the band structure calculations revealed that the three structures have a direct band gap (i.e., occurring at the Γ point). Secondly, the analysis of the geometries has shown that the α and γ structures have more rotated octahedrons along the Z axis than the β structure, whereas the β structure has larger tilting of the octahedrons. In addition to the differences in the IOF geometries, the α and γ structures also differ significantly from the β structure in terms of the orientation of the MA cations.

The experimental UV-Vis absorption spectra display variations in the absorbance with four shoulders at about 740, 660, 550 and 440 nm, which are reproduced by the simulations in the spectral regions A, B, C and D, respectively. The TD-DFT calculations allowed an assignment of the bands in the A, B and C regions, and it was shown that each region involves mainly three transitions having comparable orbital characters (Tr_1-Tr_9). Namely, the excitations involve transitions between hybridized 6s(Pb)/5p(I) orbitals and 6p(Pb) orbitals. The relative effects of the IOF and the MA cations on the absorption properties were estimated by considering the $\alpha_{IOF}\beta_{MA}$ and $\alpha_{MA}\beta_{IOF}$ structures. It was found that the spectral changes in the region A mainly originate from the modifications of the IOF between the α and

β structures, whereas the interaction with the MA cations has a stronger effect in the regions B and C. These results demonstrate that both changes in the IOF and in the MA cations orientations impact the absorption spectra (i.e., by modifying the transitions energies and intensities). These spectral differences originate from a modification of the overlap between the s(Pb), p(I) and p(Pb) orbitals (due to changes in the IOF) and from the interactions of the Pb/I electrons with different configurations of the MA cations. Therefore, it is inferred that the broad and nearly constant absorption spectrum of $MAPbI_3$, that covers the entire visible region, originates from the structural disorder at room temperature (i.e., distorted IOF and different orientations of the MA cations) that modulates the absorption properties. In particular, this study has demonstrated that the MA cations play a key role in the absorption properties despite the fact that the MA orbitals are not directly involved in the absorption transitions.

Acknowledgments

The calculations were performed at the Academic Computer Centre TASK in Gdańsk. The work has been supported by Solliance, a partnership of R&D organizations from the Netherlands, Belgium, and Germany working in thin film photovoltaic solar energy. This work is part of the research programme CLEARPV, grant M-ERA.NET 2017 CW with project number 732.017.105, which is (partly) financed by the Netherlands Organisation for Scientific Research (NWO).

Keywords

absorption spectra ; density functional theory calculations ; hybrid metal-halide perovskite ; solar cells materials ; structural properties

10.1002/cphc.201900824

Graphical abstract

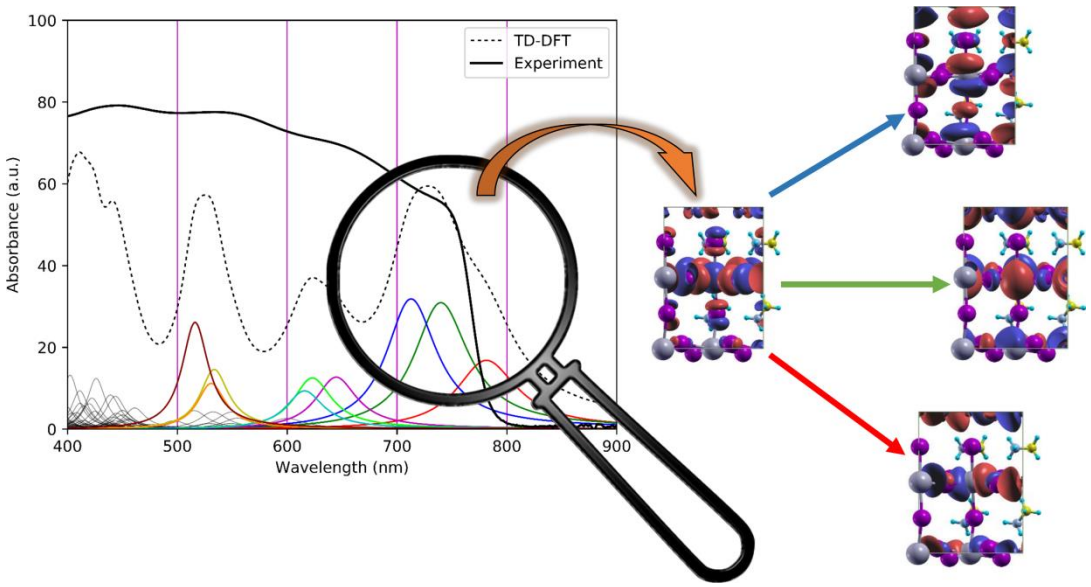

A combined theoretical and experimental study is performed in order to shed light on the nature of the electronic transitions in the absorption spectrum of the hybrid metal-halide perovskite $CH_3NH_3PbI_3$. The observed absorption shoulders are assigned by the calculations to different groups of p(I)s(Pb) → p(Pb) transitions involving the inorganic frame. Additionally, it is also shown that the orientation of the $CH_3NH_3^+$ cations has a significant impact on the transition energies and intensities explaining in part the characteristic absorbance of this material.

References

[1] H. J. Snaith, *J. Phys. Chem. Lett.* **2013**, *4*, 3623–3630.

[2] D. Weber, *Z. Naturforsch. B* **1978**, *33*, 1443–1445.

[3] A. Kojima, K. Teshima, Y. Shirai, T. Miyasaka, *J. Am. Chem. Soc.* **2009**, *131*, 6050–6051.

[4] J. Im, C. Lee, J. Lee, S. Park, N. Park, *Nanoscale* **2011**, *3*, 4088–4093.

[5] H. Kim, C. Lee, J. Im, K. Lee, T. Moehl, A. Marchioro, S. Moon, R. Humphry-Baker, J. Yum, J. E. Moser, et al., *Sci. Rep.* **2012**, *2*, 591.

[6] M. M. Lee, J. Teuscher, T. Miyasaka, T. N. Murakami, H. J. Snaith, *Science* **2012**, *338*, 643–648.

[7] J. H. Noh, S. H. Im, J. H. Heo, T. N. Mandal, S. Il Seok, *Nano Lett.* **2013**, *13*, 1764–1769.

[8] J. Burschka, N. Pellet, S.-J. Moon, R. Humphry-Baker, P. Gao, M. K. Nazeeruddin, M. Grätzel, *Nature* **2013**, *499*, 316.

[9] M. Liu, M. B. Johnston, H. J. Snaith, *Nature* **2013**, *501*, 395–398.

[10] N. J. Jeon, J. H. Noh, W. S. Yang, Y. C. Kim, S. Ryu, J. Seo, S. Il Seok, *Nature* **2015**, *517*, 476–480.

[11] H. Zhou, Q. Chen, G. Li, S. Luo, T. Song, H.-S. Duan, Z. Hong, J. You, Y. Liu, Y. Yang, *Science* **2014**, *345*, 542–546.

[12] W. S. Yang, J. H. Noh, N. J. Jeon, Y. C. Kim, S. Ryu, J. Seo, S. Il Seok, *Science* **2015**, *348*, 1234–1237.

[13] M. Saliba, T. Matsui, J.-Y. Seo, K. Domanski, J.-P. Correa-Baena, M. K. Nazeeruddin, S. M. Zakeeruddin, W. Tress, A. Abate, A. Hagfeldt, et al., *Energy Environ. Sci.* **2016**, *9*, 1989–1997.

[14] W. S. Yang, B. Park, E. H. Jung, N. J. Jeon, Y. C. Kim, D. U. Lee, S. S. Shin, J. Seo,

E. K. Kim, J. H. Noh, et al., *Science* **2017**, *356*, 1376–1379.

[15] D. Zhao, C. Wang, Z. Song, Y. Yu, C. Chen, X. Zhao, K. Zhu, Y. Yan, *ACS Energy Lett.* **2018**, *3*, 305–306.

[16] F. Brivio, A. B. Walker, A. Walsh, *APL Mater.* **2013**, *1*, 042111.

[17] E. Mosconi, A. Amat, M. K. Nazeeruddin, M. Grätzel, F. De Angelis, *J. Phys. Chem. C* **2013**, *117*, 13902–13913.

[18] C. Quarti, E. Mosconi, F. De Angelis, *Chem. Mater.* **2014**, *26*, 6557–6569.

[19] C. Quarti, E. Mosconi, F. De Angelis, *Phys. Chem. Chem. Phys.* **2015**, *17*, 9394–9409.

[20] L. D. Whalley, J. M. Frost, Y.-K. Jung, A. Walsh, *J .Chem. Phys.* **2017**, *146*, 220901.

[21] S. X. Tao, X. Cao, P. A. Bobbert, *Sci. Rep.* **2017**, *7*, 14386.

[22] J. M. Frost, K. T. Butler, A. Walsh, *APL Mater.* **2014**, *2*, 081506.

[23] A. M. A. Leguy, J. M. Frost, A. P. Mcmahon, V. G. Sakai, W. Kockelmann, C. Law, X. Li, F. Foglia, A. Walsh, B. C. O'Regan, et al., *Nat. Commun.* **2015**, *6*, 7124.

[24] M. T. Weller, O. J. Weber, P. F. Henry, A. M. Di Pumpo, T. C. Hansen, *Chem. Commun.* **2015**, *51*, 4180–4183.

[25] J. Ma, L.-W. Wang, *Nano Lett.* **2015**, *15*, 248–253.

[26] E. Mosconi, J. M. Azpiroz, F. De Angelis, *Chem. Mater.* **2015**, *27*, 4885–4892.

[27] J. M. Frost, A. Walsh, *Acc. Chem. Res.* **2016**, *49*, 528–535.

[28] J. Li, M. Bouchard, P. Reiss, D. Aldakov, S. Pouget, R. Demadrille, C. Aumaitre, B. Frick, D. Djurado, M. Rossi, et al., *J. Phys. Chem. Lett.* **2018**, *9*, 3969–3977.

[29] L. Qin, L. Lv, C. Li, L. Zhu, Q. Cui, Y. Hu, Z. Lou, F. Teng, Y. Hou, *RSC Adv.* **2017**, *7*, 15911–15916.

[30] H. Kim, J. Hunger, E. Cánovas, M. Karakus, Z. Mics, M. Grechko, D. Turchinovich, S. H. Parekh, M. Bonn, *Nat. Commun.* **2017**, *8*, 687.

[31] W. A. Saidi, S. Poncé, B. Monserrat, *J. Phys. Chem. Lett.* **2016**, *7*, 5247–5252.

[32] A. Filippetti, A. Mattoni, *Phys. Rev. B* **2014**, *89*, 125203.

[33] W.-J. Yin, T. Shi, Y. Yan, *Adv. Mater.* **2014**, *26*, 4653–4658.

[34] F. Brivio, K. T. Butler, A. Walsh, M. Van Schilfgaarde, *Phys. Rev. B* **2014**, *89*, 155204.

[35] S. De Wolf, J. Holovsky, S.-J. Moon, P. Löper, B. Niesen, M. Ledinsky, F.-J. Haug, J. Yum, C. Ballif, *J. Phys. Chem. Lett.* **2014**, *5*, 1035–1039.

[36] Y. Tian, I. G. Scheblykin, *J. Phys. Chem. Lett.* **2015**, *6*, 3466–3470.

[37] E. Mosconi, C. Quarti, T. Ivanovska, G. Ruani, F. De Angelis, *Phys. Chem. Chem. Phys.* **2014**, *16*, 16137–16144.

[38] C. Quarti, G. Grancini, E. Mosconi, P. Bruno, J. M. Ball, M. M. Lee, H. J. Snaith, A. Petrozza, F. De Angelis, *J. Phys. Chem. Lett.* **2014**, *5*, 279–284.

[39] A. Poglitsch, D. Weber, *J. Chem. Phys.* **1987**, *87*, 6373–6378.

[40] N. Onoda-Yamamuro, O. Yamamuro, T. Matsuo, H. Suga, *J. Phys. Chem. Solids* **1992**, *53*, 277–281.

[41] F. Zheng, H. Takenaka, F. Wang, N. Z. Koocher, A. M. Rappe, *J. Phys. Chem. Lett.* **2015**, *6*, 31–37.

[42] A. Mattoni, A. Filippetti, C. Caddeo, *J. Phys. Condens. Matter* **2017**, *29*, 043001.

[43] M. A. Carignano, A. Kachmar, J. Hutter, *J. Phys. Chem. C* **2015**, *119*, 8991–8997.

[44] I. Deretzis, B. N. Di Mauro, A. Alberti, G. Pellegrino, E. Smecca, A. La Magna, *Sci. Rep.* **2016**, *6*, 24443.

[45] T. Umebayashi, K. Asai, T. Kondo, A. Nakao, *Phys. Rev. B* **2003**, *67*, 155405.

[46] A. Babayigit, J. D'Haen, H.-G. Boyen, B. Conings, *Joule* **2018**, *2*, 1205–1209.

[47] P. Giannozzi, S. Baroni, N. Bonini, M. Calandra, R. Car, C. Cavazzoni, D. Ceresoli, G. L. Chiarotti, M. Cococcioni, I. Dabo, et al., *J. Phys. Condens. Matter* **2009**, *21*, 395502.

[48] J. P. Perdew, K. Burke, M. Ernzerhof, *Phys. Rev. Lett.* **1996**, *77*, 3865–3868.

[49] C. C. Stoumpos, C. D. Malliakas, M. G. Kanatzidis, *Inorg. Chem.* **2013**, *52*, 9019–9038.

[50] H. J. Monkhorst, J. D. Pack, *Phys. Rev. B* **1976**, *13*, 5188–5192.

[51] O. B. Malcioğlu, R. Gebauer, D. Rocca, S. Baroni, *Comput. Phys. Commun.* **2011**, *182*, 1744–1754.

[52] X. Ge, S. J. Binnie, D. Rocca, R. Gebauer, S. Baroni, *Comput. Phys. Commun.* **2014**, *185*, 2080–2089.

[53] D. Głowienka, T. Miruszewski, J. Szmytkowski, *Solid State Sci.* **2018**, *82*, 19–23.

[54] C. Zhu, X. Niu, Y. Fu, N. Li, C. Hu, Y. Chen, X. He, G. Na, P. Liu, H. Zai, et al., *Nat. Commun.* **2019**, *10*, 815.

[55] P. Umari, E. Mosconi, F. De Angelis, *Sci. Rep.* **2014**, *4*, 4467.

[56] C. Motta, F. El-Mellouhi, S. Sanvito, *Sci. Rep.* **2015**, *5*, 12746.